

**Small-moment antiferromagnetic ordering in single-crystalline La<sub>2</sub>Ni<sub>7</sub>**R. A. Ribeiro <sup>1,2,\*</sup>, S. L. Bud'ko <sup>1,2</sup>, L. Xiang <sup>1,2</sup>, D. H. Ryan,<sup>1,3</sup> and P. C. Canfield <sup>1,2</sup><sup>1</sup>Ames Laboratory, Iowa State University, Ames, Iowa 50011, USA<sup>2</sup>Department of Physics and Astronomy, Iowa State University, Ames, Iowa 50011, USA<sup>3</sup>The Centre for the Physics of Materials and the Physics Department, McGill University, Montreal H3A 2T8, Canada

(Received 8 October 2021; accepted 13 December 2021; published 11 January 2022)

Single crystals of La<sub>2</sub>Ni<sub>7</sub> have been grown out of a binary La-Ni melt. Temperature-dependent, zero magnetic field, specific heat, electrical resistivity, and low field magnetization measurements indicate that there is a series of antiferromagnetic (AFM) phase transitions at  $T_1 = 61.0 \pm 0.2$  K,  $T_2 = 56.5 \pm 0.2$  K, and  $T_3 = 42.2 \pm 0.2$  K. The three specific heat anomalies found at these temperatures qualitatively have very small entropy changes associated with them, and the anisotropic  $M(H)$  data saturate at  $\sim 0.12 \mu_B/\text{Ni}$ ; both observations strongly suggesting the AFM order is associated with very small, itinerant moments. Anisotropic  $H_{\parallel c}$  and  $H_{\perp c}$ ,  $\rho(H)$  and  $M(H)$  isotherms as well as constant field  $\rho(T)$  and  $M(T)$  sweeps manifest signatures of multiple phase lines and result in  $H$ - $T$  phase diagrams that are clearly anisotropic. Analysis of  $M(T)$  and  $M(H)$  data allow for the identification of the two lower temperature magnetically ordered states as AFM ordered, with the moments aligned along the crystallographic  $c$  axis, and the higher temperature  $T_2 < T < T_1$  state as having a finite ferromagnetic component. In addition, the metamagnetic transition at low temperatures, for  $H$  applied along the crystallographic  $c$  axis ( $H_{\parallel c}$ ), appears to be a near classic example of a spin-flop transition, resulting in a field stabilized AFM state with the moments ordered perpendicular to the  $c$  axis. Although the small moment ordering and existence of multiple phase transitions in field and temperature, suggesting an energetic proximity of these states, could foretell a degree of pressure sensitivity, our measurements of  $R(T)$  for applied pressures up to 2.0 GPa indicate that there is very little pressure dependence of  $T_1$ ,  $T_2$ , and  $T_3$ .

DOI: [10.1103/PhysRevB.105.014412](https://doi.org/10.1103/PhysRevB.105.014412)**I. INTRODUCTION**

Iron-based superconductors, cuprate-based superconductors, and Ce/U-based, Kondo-lattice-based superconductors all have what is thought to be exotic, non-electron-phonon-mediated superconductivity located close to the suppression of magnetic, usually antiferromagnetic (AFM), order [1]. This observation has led to the idea that the suppression of fragile magnetic states may be a necessary (but not sufficient) requirement to discovering new families of superconducting materials. A fragile magnet is one that can have the ordering temperature as well as the size of the ordered moments suppressed by perturbation (i.e., doping, pressure, or applied field) [1]. Unfortunately, whereas most rare-earth-based intermetallic compounds tend to manifest AFM order, many of the transition-metal-based metallic compounds with reduced ordered moments are ferromagnetic (FM). This is unfortunate because the avoided quantum criticality theoretically predicted and discussed over the past 20 years for metallic systems [2–8] really does seem to be an experimental reality. For example, recent systems that we examined as part of our efforts to study and understand fragile magnets: LaCrGe<sub>3</sub> [9–11], La<sub>5</sub>Co<sub>2</sub>Ge [12], and even YbFe<sub>2</sub>Zn<sub>20</sub> [13] and CeTiGe<sub>3</sub> [14] all have avoided FM quantum critical points. To this end, we have been trying to identify or discover

systems that start out as promising small-moment transition-metal-based AFMs with the intent to then use pressure and/or doping to perturb them.

Whereas La<sub>2</sub>Ni<sub>7</sub> has been known structurally since at least 1969 [15] and studied for its magnetic properties for the past several decades [16–24], it has so far only been studied in polycrystalline form. As a result of this, the existing  $H$ - $T$  phase diagrams are either an average or an admixture of the anisotropic  $H$ - $T$  phase diagrams associated with the field applied along or perpendicular to the crystallographic  $c$  axis. Buschow [16] studied La<sub>2</sub>Ni<sub>7</sub> as well as La<sub>2</sub>Ni<sub>7</sub>H<sub>x</sub>; whereas the La<sub>2</sub>Ni<sub>7</sub> was found to have a feature associated with AFM ordering below  $\sim 54$  K in its temperature-dependent Curie-Weiss (CW)-like magnetic susceptibility, the La<sub>2</sub>Ni<sub>7</sub>H<sub>x</sub> sample had very small essentially temperature-independent susceptibility data. Parker and Oesterreicher [17] identified a  $T_N$  of  $\sim 51$  K and pointed out that the paramagnetic Weiss temperature of 70 K was more consistent with a FM than an AFM. In addition, Parker and Oesterreicher [17] found that “La<sub>2</sub>Ni<sub>7</sub> exhibits the typical S-shaped magnetization versus field behavior of metamagnetic materials” and were able to construct a  $H$ - $T$  phase diagram of a single curve separating the paramagnetic from the AFM region. The paramagnetic-to-AFM phase line ran roughly from 60 kOe at base temperature to zero at  $T_N$ . Given the small high-field saturated moment of  $\sim 0.1 \mu_B/\text{Ni}$ , La<sub>2</sub>Ni<sub>7</sub> appeared to be an itinerant AFM system. Subsequently a series of papers focused on the  $M(T)$  and  $M(H)$  data [19–23] and the inferred  $H$ - $T$  phase diagram

\*ribeiro@ameslab.gov

associated with polycrystalline samples that were annealed at or near 900 °C for up to 5 wk (to get as close to single-phase hexagonal  $\text{La}_2\text{Ni}_7$  samples as possible). Initially, only a single phase line in the  $H$ - $T$  phase diagram, very similar to that seen by Parker and Oesterreicher [17], was detected. More detailed measurements [20–22] revealed two low-field phase transitions:  $\sim 66$  and  $\sim 54$  K, and a  $H$ - $T$  phase diagram with multiple regions was constructed.

One attempt was made to microscopically detect AFM ordering via powder neutron diffraction. When the experiment failed to detect any signature of the AFM order upon cooling below  $T_N$ , the authors suggested an upper limit of  $0.03 \mu_B/\text{Ni}$  [20], a value much smaller than the measured saturated moment of  $\sim 0.1 \mu_B/\text{Ni}$ . Very recently [24], computational work has predicted a  $T = 0$  K modulated AFM structure with moments of  $< 0.3 \mu_B$  (but much larger than  $0.03 \mu_B$  given by Ref. [20]) pointing along the  $c$  axis, forming FM-like blocks that alternate over a relatively long length scale.

Whereas  $M(T)$  and  $M(H)$  data have been studied by multiple groups, there is little or no other data in the literature. Temperature-dependent electrical resistivity and thermoelectric power were measured on polycrystalline  $\text{LaNi}_x$  compounds to provide  $4f^0$  (La) analogues to a study  $\text{CeNi}_x$  materials. As part of this,  $\text{La}_2\text{Ni}_7$  was measured, and data were presented in Ref. [18] without comment. There does appear to be a signature of a transition near 50 K in both electrical resistivity and thermoelectric power plots. To our knowledge, there is no published specific heat as a function of temperature data. To start to better evaluate  $\text{La}_2\text{Ni}_7$  both as a small-moment itinerant magnetic system and also as a possible fragile magnetic system, we have grown relatively large single crystals and used temperature-dependent specific heat as well as temperature- and field-dependent magnetization and electrical resistivity to determine that there are three zero-field magnetic phase transitions at  $T_1 = 61.0 \pm 0.2$  K,  $T_2 = 56.5 \pm 0.2$  K, and  $T_3 = 42.2 \pm 0.2$  K, to determine the anisotropic  $H$ - $T$  phase diagrams for  $H_{\parallel c}$  and  $H_{\perp c}$ , and to evaluate the pressure dependence of the transition temperatures for hydrostatic pressures up to 2.0 GPa.

### A. Crystal growth and La-Ni phase diagram associated with $\text{La}_2\text{Ni}_7$ formation

Single crystals of  $\text{La}_2\text{Ni}_7$  were grown out of a La-rich (relative to  $\text{La}_2\text{Ni}_7$ ) binary high-temperature melt. Elemental La (Ames Laboratory, 99.99+% pure) and Ni (Alpha, 99.9+% pure) were weighed out in a  $\text{La}_{33}\text{Ni}_{67}$  atomic ratio and placed into a tantalum crucible which was sealed with solid caps on each end and a fritted cap in the middle to act as a frit or filter for decanting [25,26]. The assembled Ta crucible was then itself sealed into an amorphous silica tube with silica wool above and below it to act as cushioning. This growth ampoule was then placed in a resistive box furnace. The furnace was then heated to 1150 °C over 10 h, held at 1150 °C for 10 h, cooled to 1020 °C over 4 h, and then very slowly cooled to 820 °C over 300 h, at which point the growth ampoule was removed and decanted in a centrifuge to separate the  $\text{La}_2\text{Ni}_7$  single crystals from the residual liquid [26]. Crystals grew as well faceted plates with clear hexagonal morphology (see insets to Fig. 1). Powder x-ray diffraction spectra (Fig. 1) were taken

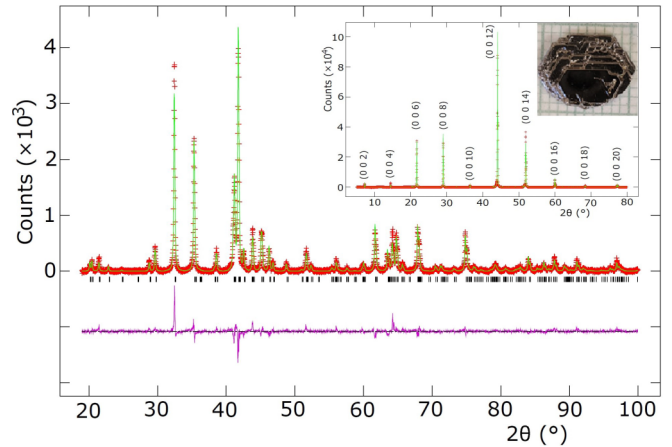


FIG. 1. Powder x-ray pattern for ground, single-crystal  $\text{La}_2\text{Ni}_7$ . Using a Rietveld refinement [27,28], the lattice parameters of  $a = 5.06352(11)$  Å and  $c = 24.6908(8)$  Å were inferred. Inset shows data from a Bragg-Brentano diffraction from a single-crystal plate demonstrating that the  $c$  axis is perpendicular to the plate. The LeBail fit to the single-crystal run gives  $c = 24.6991(3)$  Å. In both cases, the error bars result from the fitting programs used. The image is a single crystal shown over millimeter-grid graph paper.

at room temperature on a Rigaku Miniflex diffractometer with  $\text{Cu-K}\alpha$  radiation, which are well fit to the hexagonal  $\text{Ce}_2\text{Ni}_7$ , hP36, space group 194 structure [27,28].

It should be noted that (i) the above growth is the result of some degree of optimization, and (ii) solution growth is sometimes the final arbiter of disagreements between composition-temperature phase diagrams, specifically the location of liquidus lines. In our initial attempts to grow  $\text{La}_2\text{Ni}_7$ , we used the most recent La-Ni binary phase diagram in the ASM online database [29,30], which has the exposed liquidus line for  $\text{La}_2\text{Ni}_7$  existing between 63% at. Ni at 979 °C and 57% at. Ni and 802 °C. When we cooled a melt of  $\text{La}_{38}\text{Ni}_{62}$  from 1050 to 820 °C and decanted [26], we found that the melt was still in a single-phase liquid state. When we remelted the material, slow cooled, and then decanted again at 750 °C, we found a mixture of solid  $\text{LaNi}_3$  and  $\text{La}_7\text{Ni}_{16}$  (in roughly a 7:3 ratio as suggested by powder x-ray diffraction) in addition to decanted liquid. These results are inconsistent with Refs. [30,31] and suggest that the liquidus line for  $\text{La}_2\text{Ni}_7$  is shifted to higher Ni concentrations. An earlier assessment of the La-Ni binary phase diagram [32] places the liquidus line for  $\text{La}_2\text{Ni}_7$  between  $\sim 68\%$  at. Ni at 976 °C and  $\sim 65\%$  at. Ni at 811 °C. When we performed growth using a starting composition of  $\text{La}_{33}\text{Ni}_{67}$  and cooled from 1020 to 820 °C, we produced single-phase  $\text{La}_2\text{Ni}_7$  single crystals, allowing for an evaluation of the decanted liquid composition, which was  $\sim 65\%$  at. Ni. It should be noted that, for the work reported by Ref. [32], the lanthanum used was, “prepared at the Materials Preparation Center, Ames Laboratory, Iowa State University”; the same very high-purity La was used for our crystal growth.

## II. EXPERIMENTAL METHODS

Temperature-dependent specific heat  $C_p(T)$  and anisotropic temperature- and magnetic-field-dependent

measurements of electrical resistivity  $\rho(T, H)$  and magnetization  $M(T, H)$  were carried out in Quantum Design Physical Properties Measurement System (PPMS) and Magnetic Properties Measurement Systems (MPMS and MPMS3). Anisotropic dc magnetization data [ $M(T)$  in 1, 10, and 50 kOe as well as  $M(H)$  for several temperatures] were measured in MPMS classic systems, and the cascades of  $M(T)$  and  $M(H)$  curves for multiple  $H$  and  $T$  values were measured in the MPMS3 using the vibrating-sample magnometry (VSM) option. We normalized  $M(T, H)$  measured in the VSM option by the dc magnetization data to correct for potential differences in the relative accuracy of the VSM data.

Electrical resistivity was measured using a standard four-probe geometry with contacts between the sample and Pt wire made using Epotek-H20E silver epoxy. The samples were cut in long thin bars, and the measurements were performed in a Quantum Design PPMS on warming with a rate of 0.25K/min and with a current excitation of 3 mA and frequency of 17 Hz. On average, the room-temperature sample resistance was  $\sim 15$  m $\Omega$ , and the contact resistance was  $\sim 3$   $\Omega$ . The current was applied in plane (perpendicular to the crystallographic  $c$  axis) and perpendicular to the magnetic field in both  $H_{\parallel c}$  and  $H_{\perp c}$  configurations. Heat capacity measurements were made using the semiadiabatic thermal relaxation technique as implemented in the heat capacity option of the Quantum Design PPMS.

The temperature-dependent resistivity of  $\text{La}_2\text{Ni}_7$  was measured for applied hydrostatic pressures up to  $\sim 2$  GPa. The measurements were made with the current applied perpendicular to the  $c$  axis direction in a Quantum Design PPMS using a 3 mA excitation with frequency of 17 Hz on cooling rate of 0.25 K/min. A standard linear four-terminal configuration was used. The magnetic field was applied along the  $c$  axis direction. To apply pressures up to  $\sim 2$  GPa, a Be-Cu/Ni-Cr-Al hybrid piston-cylinder cell, similar to the one described in Ref. [33], was used. A 4:6 mixture of light mineral oil: n-pentane, which solidified at room temperature in the range of 3–4 GPa [33–35], was used as a pressure medium. Pressure values at low temperature were inferred from  $T_c(p)$  of elemental Pb [36,37].

### III. RESULTS

Temperature-dependent thermodynamic and transport measurements on single-crystalline  $\text{La}_2\text{Ni}_7$  reveal signatures of three distinct phase transition temperatures  $T_1 = 61.0 \pm 0.2$  K,  $T_2 = 56.5 \pm 0.2$  K, and  $T_3 = 42.2 \pm 0.2$  K. Figure 2 presents the specific heat divided by temperature  $C_p(T)/T$  as a function of temperature for  $2 \text{ K} < T < 130 \text{ K}$ . Three phase transitions are resolvable but quite small. The entropy under each feature (very roughly taken as the area between each anomaly and the extrapolated curve ignoring the anomalies) is  $< 0.001(7R \ln 2)$ ; note that there are 7 Ni per formula unit. Although this is only a qualitative evaluation of entropy, and more entropy removal would be expected at temperatures below the ordering temperatures (i.e., magnons), this small entropy removal makes it very clear that, if these are magnetic transitions, they will be associated with quite small ordered moments. A nonmagnet-

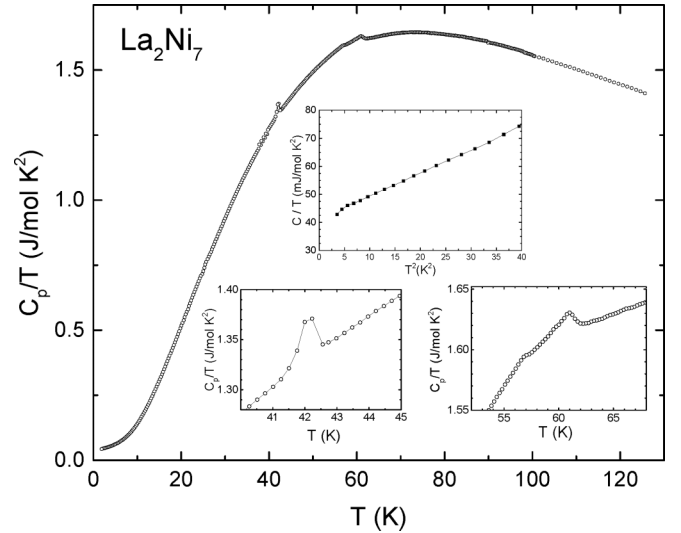


FIG. 2. Temperature-dependent specific heat divided by temperature  $C_p/T$  of  $\text{La}_2\text{Ni}_7$  for  $2 \text{ K} < T < 125 \text{ K}$ . Upper inset, plot of  $C_p/T$  vs  $T^2$  for  $T^2 < 40 \text{ K}^2$ . Lower left inset, expanded view for  $40 \text{ K} < T < 45 \text{ K}$ ; lower right inset, expanded view for  $50 \text{ K} < T < 70 \text{ K}$ .

ically ordering, isostructural analogue would be needed for a more accurate evaluation of entropy changes, and unfortunately, one is not readily available. At low temperatures, the specific heat follows a  $C(T) = \gamma T + \beta T^3$  temperature dependence for  $T^2 < 40 \text{ K}^2$  (upper inset), giving  $\gamma \sim 40 \text{ mJ}/(\text{mol K}^2)$  and  $\beta = 0.83 \text{ mJ}/(\text{mol K}^4)$ , which gives a Debye temperature of  $\sim 280$  K. Whereas the Sommerfeld coefficient  $\gamma \sim 40 \text{ mJ}/(\text{mol K}^2)$  has a somewhat high value for a compound with 7 Ni or 9 atoms total per formula unit, i.e.,  $5.7 \text{ mJ}/(\text{mol-Ni T}^2)$  or  $4.4 \text{ mJ}/(\text{mol-atomic T}^2)$ , this value is being extracted well below the ordering temperatures, after the entropy removal associated with the magnetic ordering. With these caveats, some enhancement of the Sommerfeld coefficient  $\gamma$  was suggested by the recent band structure calculations in Ref. [24], which found an enhanced density of states (DOS) at the Fermi energy ( $E_F$ ).

Figure 3 presents the temperature-dependent electrical resistivity  $\rho(T)$  for  $2 \text{ K} < T < 300 \text{ K}$  for two crystals with the current flowing perpendicular to the  $c$  axis. The difference in inferred resistivity values is a measure of the geometric uncertainties in the distance between the voltage contacts and the cross-sectional area. The upper inset shows an expanded view for  $30 \text{ K} < T < 70 \text{ K}$ . Whereas there is a clear loss of spin disorder scattering seen in the  $\rho(T)$  data upon cooling through  $\sim 65 \text{ K}$ , the  $d\rho(T)/dT$  data show three clear transition temperatures [38]. The residual resistivity ratio  $\text{RRR} = \rho(300 \text{ K})/\rho(2 \text{ K}) > 18$ , indicating a relatively small amount of disorder scattering.

Figure 4 presents the anisotropic  $H = 1 \text{ kOe}$ , temperature-dependent magnetization divided by applied field  $M(T)/H$ , as well as the polycrystalline average  $(M/H)_{\text{poly}} = \frac{1}{3}(M/H_{\parallel c}) + \frac{2}{3}(M/H_{\perp c})$ . The inset to Fig. 4 shows an expanded view for  $35 \text{ K} < T < 75 \text{ K}$ . Whereas for  $M/H_{\parallel c}$ , three transition tem-

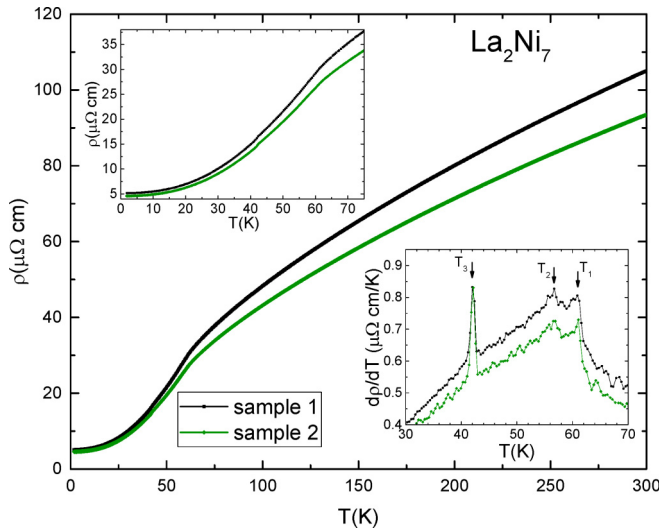


FIG. 3. Temperature-dependent electrical resistivity of two samples of  $\text{La}_2\text{Ni}_7$  for  $2\text{ K} < T < 300\text{ K}$ . The different values of resistivity are representative of our geometric uncertainties in length between voltage contacts as well as the cross-sectional area of the samples. Upper inset, expanded view for  $2\text{ K} < T < 70\text{ K}$ ; lower inset:  $d\rho(T)/dT$  plotted for  $30\text{ K} < T < 70\text{ K}$  with transition temperatures  $T_1$ ,  $T_2$ , and  $T_3$  indicated by arrows.

peratures are readily seen, for  $M/H_{\perp c}$ , the signatures of the phase transitions are more subtle, especially the lowest  $\sim 42\text{ K}$  one. Here,  $(M/H)_{\text{poly}}$  can be fit to a CW,  $C/(T + \theta) + \chi_0$ , temperature dependence, with a temperature-independent  $\chi_0$  for  $70\text{ K} < T < 300\text{ K}$ . From this fit, we find  $\theta = -54.8(5)\text{ K}$ ,  $\chi_0 = 1.01(5) \times 10^{-3}\text{ emu/mol-Ni}$ , and from  $C = 0.204(5)\text{ emu K/mol-Ni}$ , we get  $\mu_{\text{eff}} = 1.28(5)\mu_{\text{B}}/\text{Ni}$ , a

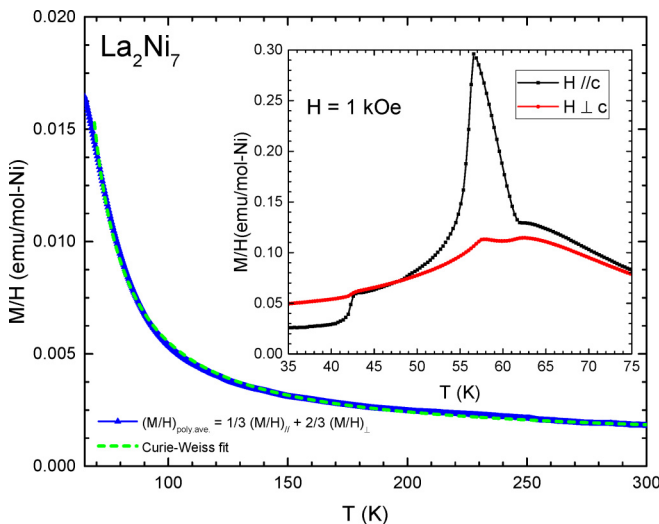


FIG. 4. Temperature-dependent, anisotropic, low field magnetization divided by applied field  $M(T)/H$  for  $2\text{ K} < T < 300\text{ K}$  for field applied along the  $c$  axis  $M/H_{\parallel c}$ , for the field applied perpendicular to the  $c$  axis  $M/H_{\perp c}$ , and for  $(M/H)_{\text{poly}} = \frac{1}{3}(M/H_{\parallel c}) + \frac{2}{3}(M/H_{\perp c})$ . The green dashed line is a Curie-Weiss fit to the  $(M/H)_{\text{poly}}$  data (see text). Inset shows an expanded view of  $35\text{ K} < T < 75\text{ K}$ .

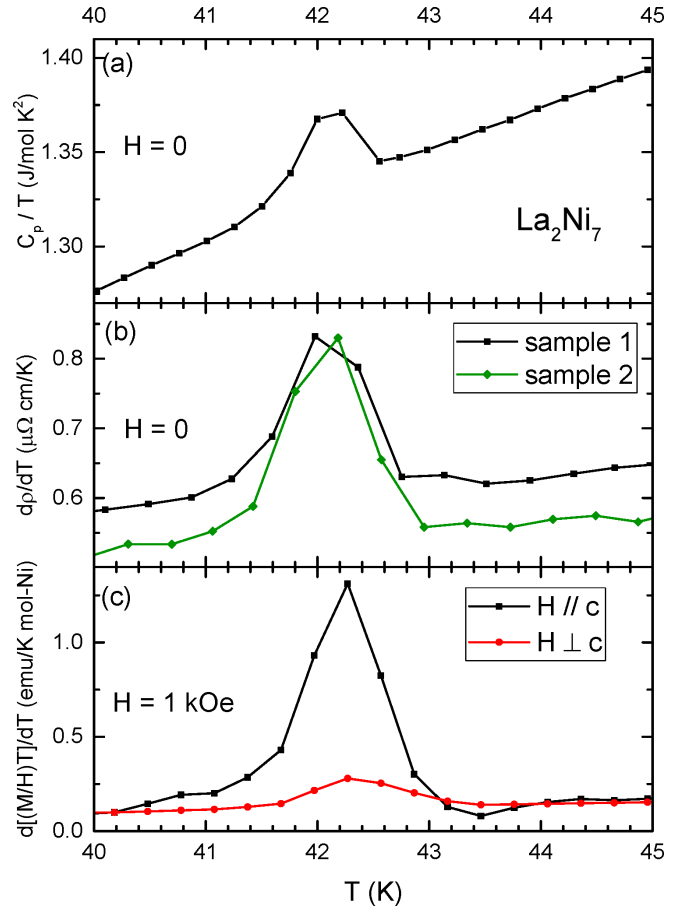


FIG. 5.  $C_p/T$ ,  $d\rho/dT$ ,  $d\{[M(H)T]/dT$  data for  $40\text{ K} < T < 45\text{ K}$ .

value comparable but somewhat larger than found in earlier polycrystalline measurements [17]. Between the highest ordering temperature  $T_1 = 61$  and  $70\text{ K}$ , there is a clear non-CW behavior.

To determine the values of the three transition temperatures, in Figs. 5 and 6, we compare the  $C(T)$ ,  $d\rho(T)/dT$  [38] and  $d\{[M(T)/H]T\}/dT$  [39] data in the vicinity of the transitions; whereas  $d\rho(T)/dT$  and  $d\{[M(T)/H]T\}/dT$  are related to  $C_p(T)$  in the vicinity of a paramagnetic-to-AFM phase transition, they can be helpful in identifying phase transition temperatures for cascades of magnetic transitions [40–42]. Figure 5 shows the features associated with the lowest transition  $T_3$ , with a clear peak seen in all three datasets. The transition temperature is inferred from the position of the local maximum, giving a value of  $T_3 = 42.2 \pm 0.2\text{ K}$ . In Fig. 6, the signatures of the upper two transitions are shown. For  $C_p(T)/T$  and  $d\rho(T)/dT$ , there are well-resolved peaks with maxima located at  $T_1 = 61.0 \pm 0.2\text{ K}$  and  $T_2 = 56.5 \pm 0.2\text{ K}$ . Whereas for  $T_3$  there is fair agreement between the value of the transition temperature inferred from  $C_p(T)/T$  and  $d\rho(T)/dT$  and the transition temperature inferred from  $d\{[M(T)/H]T\}/dT$ , for  $T_2$  and  $T_1$ , the features in  $d\{[M(T)/H]T\}/dT$ , especially for the  $H_{\parallel c}$  data, are somewhat shifted. As will be discussed below, the magnetization data for  $H_{\parallel c}$  indicate that, between  $T_1$  and  $T_2$ , the low-field state has a FM component, making the use of

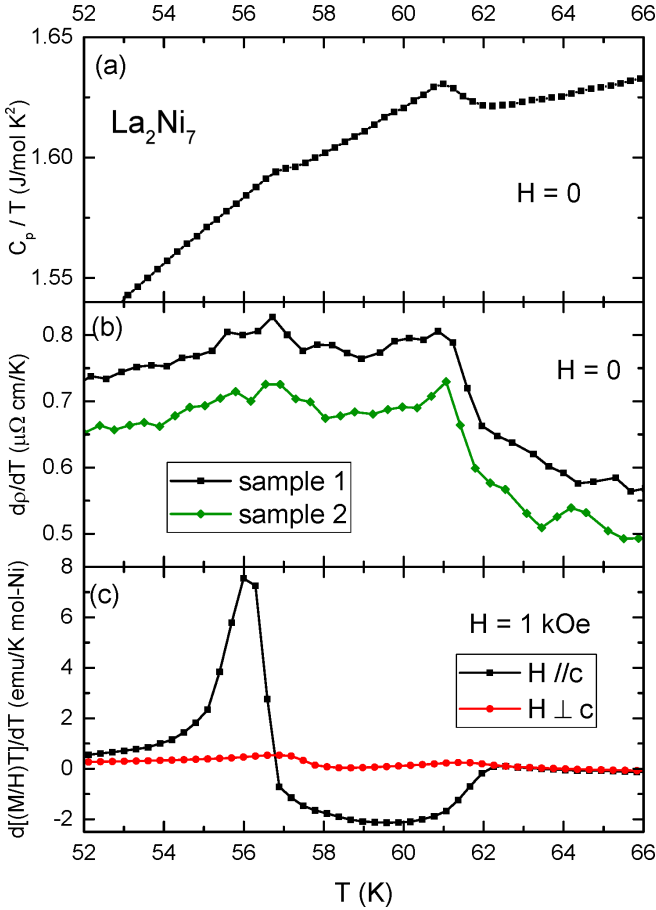


FIG. 6.  $C_p/T$ ,  $d\rho/dT$ ,  $d\{[M(H)T]/dT\}$  data for  $52\text{ K} < T < 66\text{ K}$ .

$d\{[M(T)/H]T\}/dT$  to determine a transition into or out of this state a little less accurate. In total then, based on these data,  $\text{La}_2\text{Ni}_7$  has three transitions upon cooling in zero (or low)-field:  $T_1 = 61.0 \pm 0.2\text{ K}$ ,  $T_2 = 56.5 \pm 0.2\text{ K}$ , and  $T_3 = 42.2 \pm 0.2\text{ K}$ .

#### IV. MAGNETIC FIELD-TEMPERATURE PHASE DIAGRAMS

All prior  $H$ - $T$  phase diagram work has been based on polycrystalline samples that have had either only one or, at most, two low-field transition temperatures identified. Given that  $H$ - $T$  phase diagrams of systems that have multiple potentially complex and/or fragile magnetic phases are often anisotropic, the use of single-crystalline samples is strongly preferred. In Figs. 7(a) and 7(b), we present the  $H$ - $T$  phase diagram for  $H_{\parallel c}$  and  $H_{\perp c}$ . These phase diagrams were inferred from the  $R(H)$  and  $M(H)$  isothermal sweeps as well as  $R(T)$  and  $M(T)$  constant field sweeps shown in Figs. 8–17 below. In Figs. 7(a) and 7(b), the error bars are defined as full width at half maximum of the derivatives; those are a combination of chosen criterion and the error bars. The values extracted from magnetization measurements that have error bars smaller than the point sizes for  $M(H)$  are 2 kOe, for  $M(T)$  are 0.5 K approximately. The values extracted from  $R(H)$  have an error bar of  $\sim 5\text{ kOe}$  for all transitions and

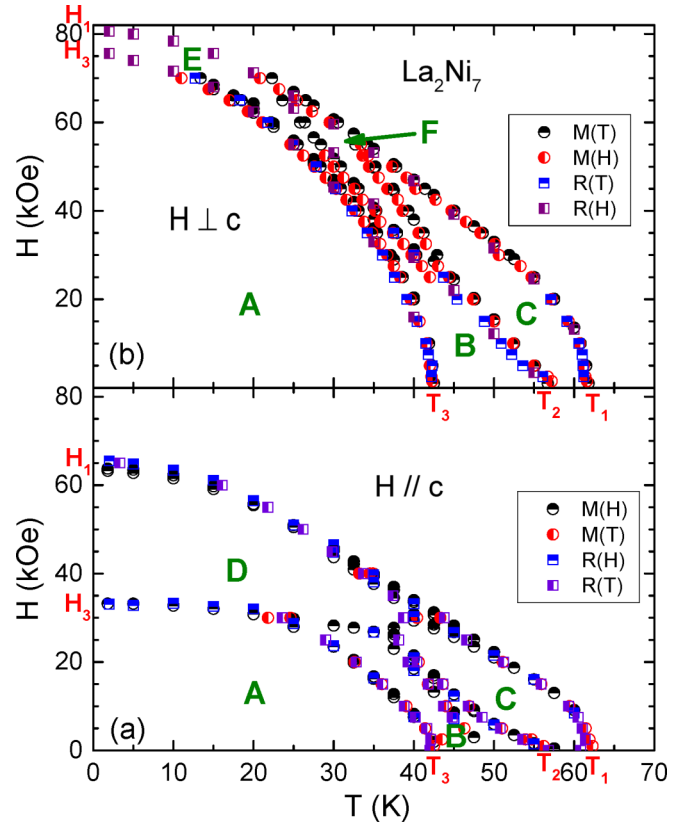


FIG. 7.  $H$ - $T$  phase diagrams for  $\text{La}_2\text{Ni}_7$  (a) for  $H_{\parallel c}$ , (b) for  $H_{\perp c}$  constructed from  $M(T)$ ,  $M(H)$ ,  $\rho(T)$ , and  $\rho(H)$  data with  $T$  or  $H$  increasing. Zero-field transition temperatures:  $T_1 = 61.0 \pm 0.2\text{ K}$ ,  $T_2 = 56.5 \pm 0.2\text{ K}$ , and  $T_3 = 42.2 \pm 0.2\text{ K}$  are shown along the horizontal axis; low temperature, anisotropic, metamagnetic fields  $H_1$  and  $H_3$  are shown along the vertical axis. Whereas the A, B, and C phases must be the same in the lowest field limit, the phases D, E, and F exist only at finite fields and need to be examined individually, see text for details.

from  $R(T)$  have a different error bar for each transition:  $T_3 \leq 0.4\text{ K}$ ,  $T_2 \leq 1.2\text{ K}$ , and  $T_1 \leq 0.6\text{ K}$ . Each of these datasets will be discussed in detail in the text and figures below. From these data, we have been able to identify and track multiple transitions with resolvable and intelligible features. There are also smaller features or more subtle transitions that we do not completely identify; some of these are discussed and commented on in the text below. The aim of this paper is to lay out the primary features of these anisotropic phase diagrams. Clearly, further work and study will be needed to fully delineate and understand the  $\text{La}_2\text{Ni}_7$  system. Figure 8(a) presents the  $M(H_{\parallel c})$  data for increasing field. There is an intelligible complexity to the primary features associated with these curves; three primary phase lines can be seen evolving in the  $M(H)$  data. The transition to the saturated paramagnetic state is located near 63 kOe at base temperature and moves monotonically downward with increasing temperature until it is no longer resolvable near  $T_1$ . The second low-temperature transition near 30 kOe is relatively temperature insensitive for  $2\text{ K} < T < 20\text{ K}$  but then splits into two transition features with one decreasing to  $H = 0$  near  $T_2$ , the other decreasing to  $H = 0$  near  $T_3$ . All these features are quite visible in the  $M(H)$  data, and transition fields are identified via maxima in

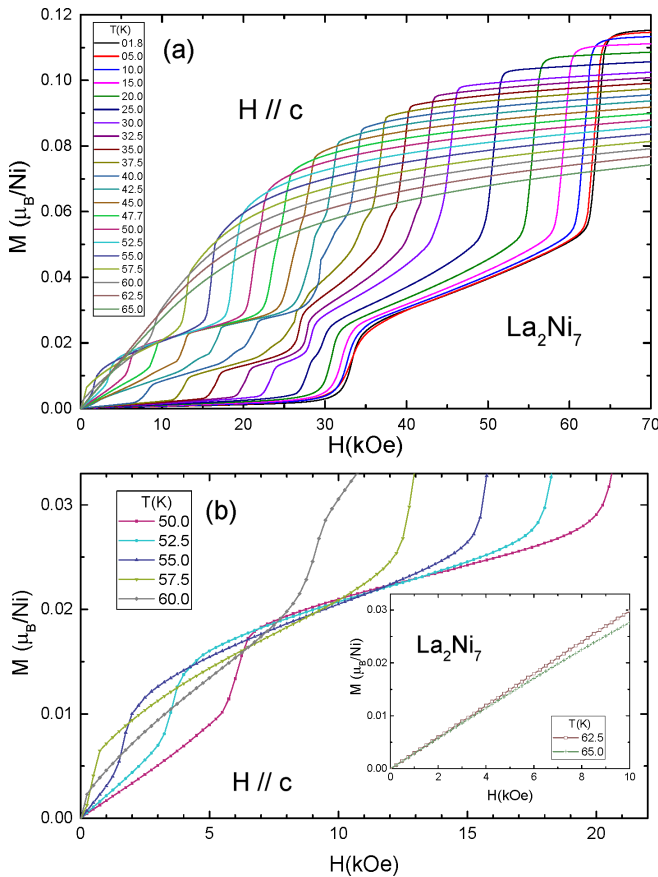


FIG. 8. (a)  $M(H)$  isotherms for  $H_{||c} < 70$  kOe (field increasing) and for selected  $T$  in the  $1.8 \text{ K} \leftarrow T \leftarrow 65 \text{ K}$  range; (b)  $M(H)$  isotherms for  $H_{||c} < 22$  kOe and for selected  $T$  in the  $50 \text{ K} \leftarrow T \leftarrow 60 \text{ K}$  range; inset:  $M(H)$  isotherms for  $H_{||c} < 10$  kOe and for selected  $T = 62.5$  and  $65 \text{ K}$ .

analysis of  $dM/dH$  plots (not shown). In addition to the three primary lines mentioned above, there is an apparent separation of the line that extrapolates to  $T_2$  as it drops from 20 kOe toward  $H = 0$ . Although this line would seem to extrapolate to  $H = 0$  near 50 K, there are no signatures of a transition at this temperature in either  $C_p(T)$ ,  $\rho(T)$ , or lower field  $M(T)/H$  data. This suggests that there may be a missing low-field dome in this region, but it is not readily resolved or systematically followed.

Figure 8(b) presents an expanded view of the higher temperature, lower field  $M(H_{||c})$  data. If we start with the 50 K data near 20 kOe (upper right corner of the figure), we can see the transition to paramagnetic/saturated paramagnetic state into the C phase; near 6 kOe, there is a transition from the C phase into the lower field B state. As temperature increases to 52.5 K and then 55 K, both transition fields decrease. At 55 K, there is still a small low-field region of  $M(H)$  data with a lower slope that can be associated with the B phase, followed by the steplike rise in  $M(H)$  associated with the transition into the C phase. All these data consistently suggest that the C phase has a finite, net FM component to its ordered state. The  $M(H)$  data for 57.5 and 60 K have a low-field saturation that is consistent with being in the C phase from the lowest measured field. Indeed, this is consistent with the low-field  $M(T)$  data shown in Fig. 4 above as well as Fig. 12 below.

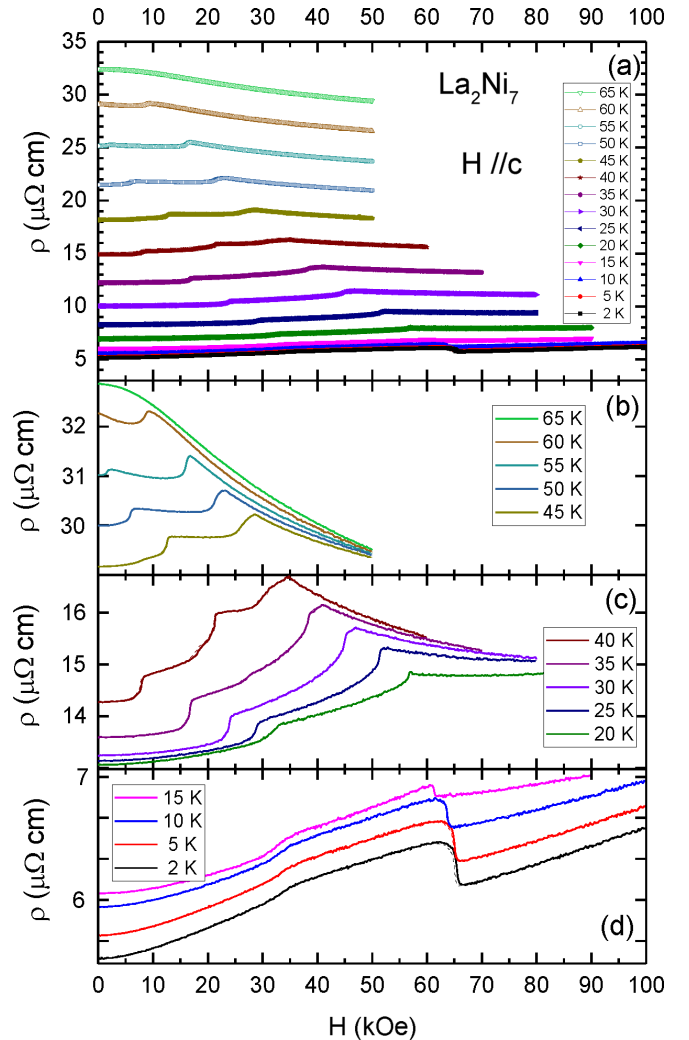


FIG. 9. (a)  $\rho(H)$  isotherms for  $H_{||c} < 100$  kOe and for selected  $T$  in the  $2 \text{ K} \leftarrow T \leftarrow 65 \text{ K}$  range; (b)  $\rho(H)$  isotherms for  $H_{||c} < 50$  kOe and for  $T = 45, 50, 55, 60,$  and  $65 \text{ K}$  with  $T = 45, 50, 55,$  and  $60 \text{ K}$  data shifted along the y axis for clarity; (c)  $\rho(H)$  isotherms for  $H_{||c} < 80$  kOe and for  $T = 20, 25, 30, 35,$  and  $40 \text{ K}$  with  $T = 20, 25, 30,$  and  $35 \text{ K}$  data shifted along the y axis for clarity; (d)  $\rho(H)$  isotherms for  $H_{||c} < 100$  kOe and for  $T = 2, 5, 10,$  and  $15 \text{ K}$  with  $T = 2, 5,$  and  $10 \text{ K}$  data shifted along the y axis for clarity. Data taken on decreasing field are shown with dashed lines.

Figure 9 presents the  $\rho(H_{||c})$  data; given that there is significant temperature dependence of the zero-field  $\rho(T)$ , the  $\rho(H)$  isotherms separate from each other rather naturally [Fig. 9(a)]. At the lowest temperatures [Fig. 9(d)], there are two clear transitions visible in the  $\rho(H)$  data, one between 30 and 35 kOe and the other between 60 and 65 kOe. As temperature rises, both transition fields decrease. For  $T = 40 \text{ K}$ , Fig. 9(c), three phase transition features are seen, and for higher temperatures, Fig. 9(b), two features are resolved up to 55 K; at 60 K, only one feature is seen, and for 65 K, no features in  $\rho(H)$  are resolved. As can be seen in Fig. 7(a), the transition fields inferred from the  $M(H)$  and  $\rho(H)$  data agree with each other very well.

Figure 10 presents the  $M(H_{\perp c})$  isotherm data for increasing field. Having already understood the  $M(H_{||c})$  data in Fig. 8,

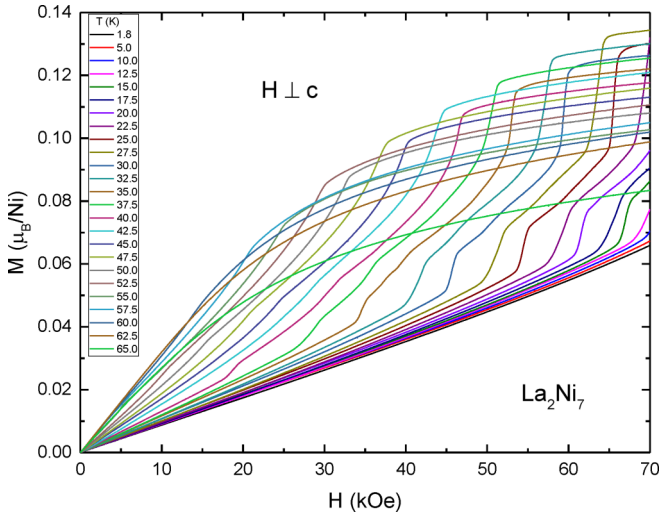


FIG. 10.  $M(H)$  isotherms for  $H_{\perp c} < 70$  kOe (field increasing) and for selected  $T$  in the  $1.8 \text{ K} \leftarrow T \leftarrow 65 \text{ K}$  range.

and tracking three phase lines as they go to  $H = 0$  as  $T$  increases, we can follow a similar strategy for the  $M(H_{\perp c})$  data. Given that the critical fields needed to induce metamagnetic phase transitions shift to higher values for  $H_{\perp c}$ , the transition to the saturated paramagnetic state only comes into our 70 kOe range for  $T = 22.5 \text{ K}$ . As temperature is increased to higher values, this highest field metamagnetic phase transition is induced at lower and lower values of applied field, reaching  $H = 0$  near  $T_1$ . The  $T = 22.5 \text{ K}$  data also show a lower field transition near 60 kOe. This feature moves up in field for lower temperatures, just barely manifesting below 70 kOe for 12.5 K. As temperature increase above 22.5 K, the lower field transition moves down in field and separates into two broad features, clearly seen, for example, in the 37.5 K isotherm. These two features head toward  $H = 0$  at different rates with one phase line extrapolating toward  $T_2$  and the other toward  $T_3$ . As was the case for the data shown in Fig. 8, all these features are quite visible in the  $M(H)$  data, and transition fields are identified via maxima in analysis of  $dM/dH$  plots (not shown). In addition to these more conspicuous features, there appear to be a pair of phase lines running from the lower field  $T_2$  or  $T_3$  lines up to the  $T_1$  line for intermediate fields and temperatures.

Figure 11 presents the  $R(H_{\perp c})$  isotherm data; again, the temperature dependence of the zero-field resistivity data leads to a natural offset between the isotherms. From  $T = 2$  to 20 K [Fig. 11(d)], there are two distinct features, starting  $\sim 80$  and 75 kOe at base temperature and decreasing to  $\sim 72$  and  $\sim 62$  kOe by 20 K. It should be noted that the lower of these two transitions manifests clear field-up/field-down hysteresis that grows smaller with increasing temperature (similar but smaller hysteresis can also be seen in Fig. 9). For  $T = 25$  to 45 K [Fig. 11(c)], there are three transitions observable, in some cases with the middle transition only clearly revealing itself by comparing field-up and field-down curves and letting the hysteresis highlight the subtle feature. In Fig. 11(b), there are two features visible for  $T = 50$  and 55 K and a single feature visible for  $T = 60 \text{ K}$ . As can be seen in Fig. 7(b), the

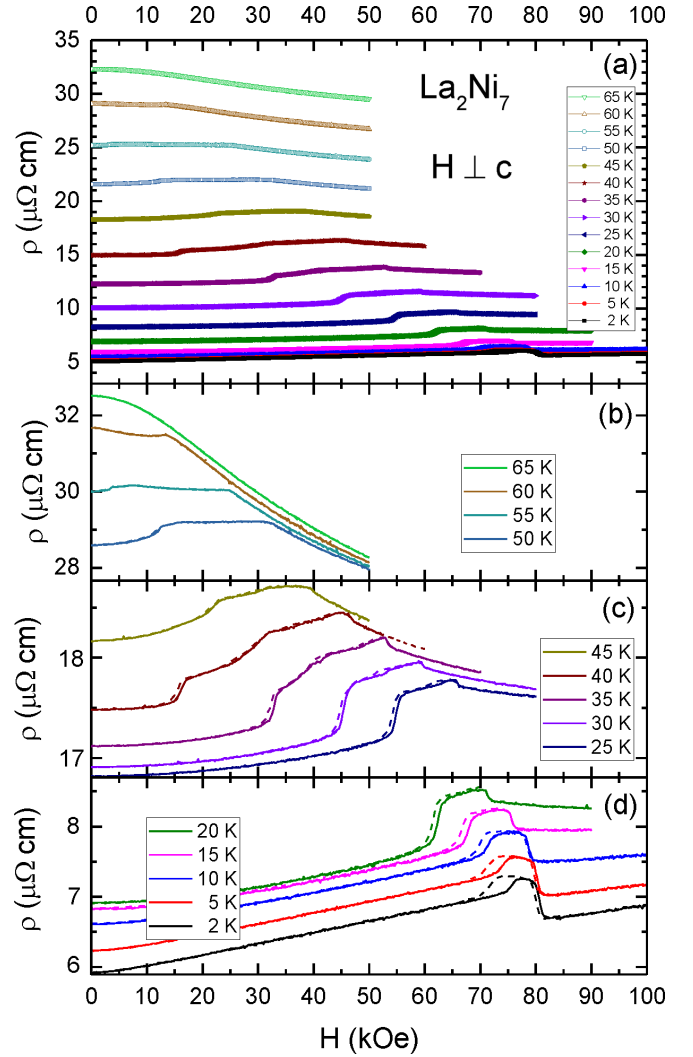


FIG. 11. (a)  $\rho(H)$  isotherms for  $H_{\perp c} < 100$  kOe and for selected  $T$  in the  $2 \text{ K} \leftarrow T \leftarrow 65 \text{ K}$  range; (b)  $\rho(H)$  isotherms for  $H_{\perp c} < 50$  kOe and for  $T = 50, 55, 60,$  and  $65 \text{ K}$  with  $T = 50, 55,$  and  $60 \text{ K}$  data shifted along the y axis for clarity; (c)  $\rho(H)$  isotherms for  $H_{\perp c} < 80$  kOe and for  $T = 25, 30, 35, 40,$  and  $45 \text{ K}$  with  $T = 25, 30, 35,$  and  $40 \text{ K}$  data shifted along the y axis for clarity; (d)  $\rho(H)$  isotherms for  $H_{\perp c} < 100$  kOe and for  $T = 2, 5, 10, 15,$  and  $20 \text{ K}$  with  $T = 2, 5, 10,$  and  $15 \text{ K}$  data shifted along the y axis for clarity. Data taken on decreasing field are shown with dashed lines.

transition fields inferred from the  $M(H)$  and  $\rho(H)$  data agree with each other very well.

Whereas the  $M(H)$  and  $\rho(H)$  isotherm data tend to be more sensitive to  $H$ - $T$  phase lines that are more horizontal in nature and therefore often offer greater detail for the lower temperature parts of the phase diagram, the constant magnetic field  $M(T)$  and  $\rho(T)$  data tend to be more sensitive to phase lines that are more vertical in nature and therefore often offer greater detail for the higher temperature parts of the phase diagram. In Fig. 12, the  $M(T)/H$  sweeps at constant  $H_{\perp c}$  are shown for fields ranging from 1 to 65 kOe. The  $(H, T)$  data points we extract from these measurements via identification of extrema in  $d\{[M(T)/H]T\}/dT$  plots (not shown) agree well with the  $M(H)$  and  $\rho(H)$  data point already appearing in

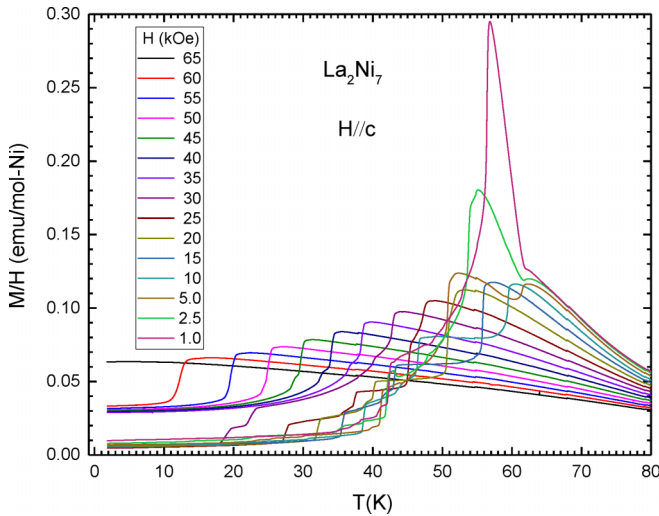


FIG. 12.  $M(T)/H_{||c}$  data for  $1.8 \text{ K} \leq T \leq 80 \text{ K}$  (temperature increasing) and selected fields  $1 \text{ kOe} \leq H_{||c} \leq 65 \text{ kOe}$ .

Fig. 7(a). Starting at highest fields and low temperatures, we can see the  $T_1$  line as a sharp transition from the ordered state into the paramagnetic state (or saturating paramagnetic state) move from  $\sim 12 \text{ K}$  at  $60 \text{ kOe}$  up to just under  $T_1$  at  $1 \text{ kOe}$ . For applied fields of  $30 \text{ kOe}$  and below, the  $T_3$  and  $T_2$  lines and the associated features in the  $M(T)$  data become apparent. A pair of lower temperature steps in the  $M(T)$  data move upward in temperature as the applied field decreases, reaching just below  $T_3$  and  $T_2$  for  $H_{||c} = 1 \text{ kOe}$ . There are finer features in the  $M(T)$  data shown in Fig. 12 that we show in Fig. 7(a), such as the slight splitting of the  $T_1$  line in the  $25\text{--}40 \text{ K}$  region. These may delineate very narrow regions of other phases or may be artifacts that we do not yet understand. For this first determination of the anisotropic  $H\text{-}T$  phase diagrams, we will focus on the more conspicuous and less ambiguous features in

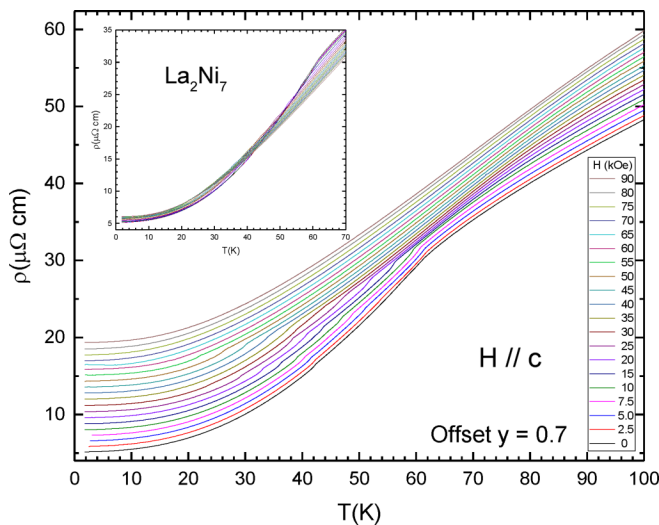


FIG. 13.  $\rho(T, H_{||c})$  data for  $2 \text{ K} \leq T \leq 100 \text{ K}$  (temperature increasing) and selected fields  $0 \text{ kOe} \leq H_{||c} \leq 90 \text{ kOe}$ . Data curves in the main figure are offset from each other by  $0.7 \mu\Omega\text{-cm}$  for clarity, whereas the curves in the inset are not offset.

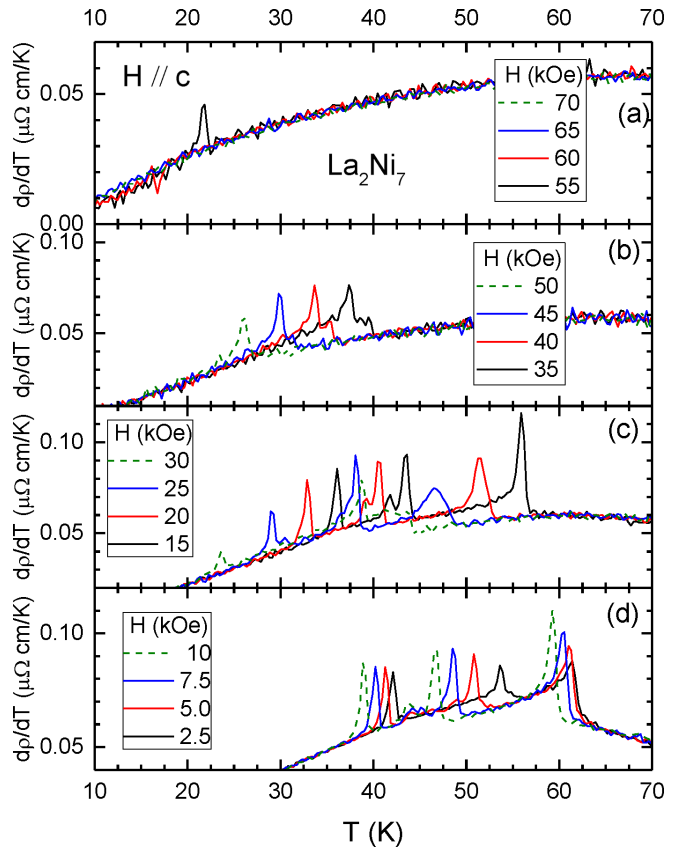


FIG. 14.  $d\rho/dT$  plots for data shown in Fig. 13.

our data. As will be discussed below, there may well be further work needed to fully understand the interplay between all the phases that may exist in  $\text{La}_2\text{Ni}_7$ . As discussed above, with regard to Fig. 8(b), the C phase appears to have a well-defined FM component to its ordering. This is particularly apparent in the lowest field  $M(T)$  data for  $T_2 < T < T_1$ .

In Fig. 13, we present  $\rho(T)$  data taken for differing  $H_{||c}$  values, and in Fig. 14, we present the  $d\rho(T)/dT$  data. Given

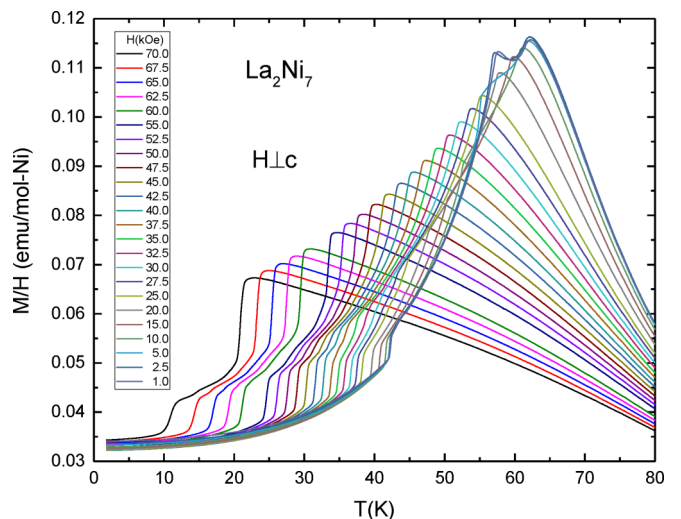


FIG. 15.  $M(T)/H_{\perp c}$  data for  $1.8 \text{ K} \leq T \leq 80 \text{ K}$  (temperature increasing) and selected fields  $1 \text{ kOe} \leq H_{\perp c} \leq 70 \text{ kOe}$ .

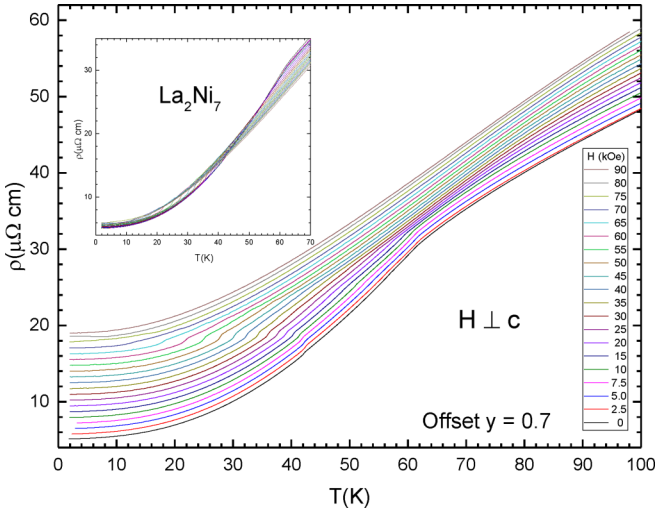


FIG. 16.  $\rho(T)/H_{\perp c}$  data for  $1.8 \text{ K} \leq T \leq 100 \text{ K}$  (temperature increasing) and selected fields  $0 \text{ kOe} \leq H_{\parallel c} \leq 90 \text{ kOe}$ . Data curves in the main figure are offset from each other by  $0.7 \mu\Omega\text{-cm}$  for clarity, whereas the curves in the inset are not offset.

that (i) the  $\rho(T)$  data change a lot over the  $2 \text{ K} < T < 70 \text{ K}$  temperature range and (ii) the effects of magnetic ordering as well as applied field are resolvable but small compared with the temperature dependence, it is difficult to see the systematic effects of applied field in the bare  $\rho(T)$  data. In Fig. 14, the  $d\rho(T)/dT$  data reveal a systematic shift of transitions with

applied field, and using the local maxima to identify critical temperatures, we can see very good agreement with the other  $(H, T)$  data in Fig. 7(a). We can again see the three primary  $T_1$ ,  $T_2$ , and  $T_3$  lines as well as some of the finer structure we found in our other measurements. It is worth noting that the  $\rho(T)$  data for  $H_{\parallel c} = 60$  and  $65 \text{ kOe}$  do not clearly reveal the  $T_1$  phase line; this is not unusual, given that, as mentioned earlier,  $\rho(T)$  data better reveal the more vertical lines on an  $H$ - $T$  phase diagram with the  $\rho(H)$  data more clearly revealing the more horizontal ones.

Similar data can be collected and analyzed for the  $H_{\perp c}$  direction. Figure 15 presents  $M(T)/H$  data for constant  $H_{\perp c}$ . Starting at our highest applied field  $70 \text{ kOe}$ , there are two clear transitions visible in the  $M(T)$  data that, from  $d\{[M(T)/H]T\}/dT$  plots, can have transition temperatures of  $11$  and  $21 \text{ K}$  identified. The higher temperature feature increases in temperature as  $H_{\perp c}$  is decreased, ending up at  $\sim T_1$  for  $H_{\perp c} = 1 \text{ kOe}$ . The lower temperature feature also moves up in temperature as  $H_{\perp c}$  is decreased, reaching  $T_3$  for  $H_{\perp c} = 1 \text{ kOe}$ . For fields between  $70$  and  $55 \text{ kOe}$ , two distinct features can be seen in the  $M(T)$  data; below  $55 \text{ kOe}$ , a third and sometimes a somewhat less distinct fourth or fifth feature can be seen. Below  $30 \text{ kOe}$ , three dominant well-defined features separate and become clear with the middle one ending near  $T_2$  for  $H_{\perp c} = 1 \text{ kOe}$ . These data are plotted in Fig. 7(b) and agree well with the data extracted from the  $M(H)$  and  $\rho(H)$  sweeps. As has been mentioned before, there are some finer structures in the  $M(T)/H$  data for constant  $H_{\perp c}$  that we are not currently quantifying; these may at some future date reveal further structures.

In Fig. 16, we present  $\rho(T)$  data taken for differing  $H_{\perp c}$  values, and in Fig. 17, we present the  $d\rho(T)/dT$  data. These data reveal well-defined features that allow for the identification of transition temperatures. At highest fields, a single transition becomes detectable for  $H = 65 \text{ kOe}$  and moves up in temperature as the field is decreased to  $45 \text{ kOe}$ . The extracted transition temperatures match well with the  $T_3$  line. It is worth noting that  $\rho(T)$  does not seem to be sensitive to the higher temperature features that were detected by our other measurements, again illustrating the need to use multiple types of measurements and sweeps to fully determine a  $H$ - $T$  phase diagram. As the field is lowered below  $45 \text{ kOe}$ , two and then ultimately three distinct features emerge, ultimately clearly separating into the  $T_3$ ,  $T_2$ , and  $T_1$  lines. Figures 7(a) and 7(b) show the general good agreement between all the data points determined from the  $\rho(H)$ ,  $M(H)$ ,  $\rho(T)$ , and  $M(T)/H$  datasets.

### A. Pressure dependence of transition temperatures

To make an initial assessment of the pressure sensitivity of  $\text{La}_2\text{Ni}_7$ , we measured the temperature-dependent electrical resistance for applied pressures  $p < 2 \text{ GPa}$  in a self-clamping piston-cylinder cell. In Fig. 18, we show  $R(T)$  for  $2 \text{ K} < T < 300 \text{ K}$  with the upper inset showing an expanded range centered on  $42 \text{ K}$  and the lower inset showing an expanded range centered on  $60 \text{ K}$ . These data immediately reveal that the three phase transitions as well as the temperature-dependent resistance data as a whole are not very sensitive to pressures up to  $2 \text{ GPa}$ . Figure 19 presents the  $dR(T)/dT$  plots for

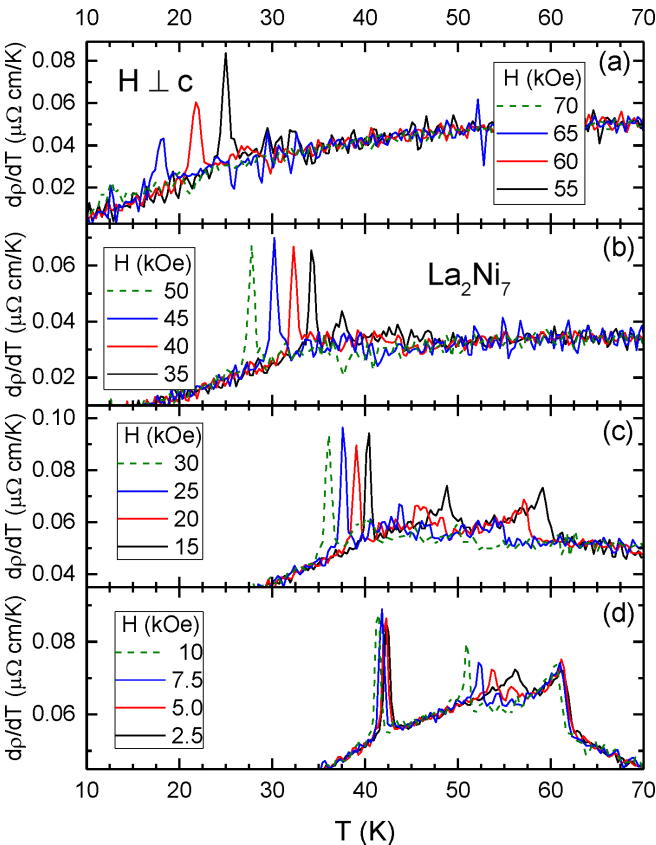


FIG. 17.  $d\rho/dT$  plots for data shown in Fig. 16.

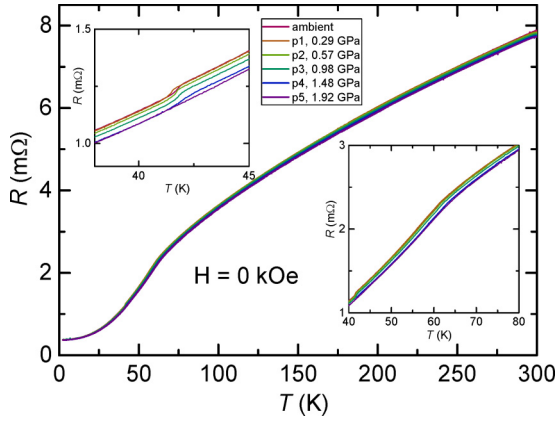


FIG. 18. Temperature-dependent resistance  $R(T)$  of  $\text{La}_2\text{Ni}_7$  for applied pressures  $p < 2.0$  GPa; upper inset: expanded view centered on 42 K, lower inset: expanded view centered on 60 K.

$20 \text{ K} < T < 80 \text{ K}$  for the data shown in Fig. 18. For most pressures, we can resolve features associated with the three phase transitions. In Fig. 20, we plot the pressure dependence of the three magnetic phase transition temperatures; indeed, as was already suggested by Figs. 18 and 19, there is very little change in the transition temperatures with pressure. Given that the position and sharpness of these features can change with applied field, in Fig. 21(a), we plot  $R(T)$  for  $30 \text{ K} < T < 65 \text{ K}$  with a field of 10 kOe applied along the  $c$  axis; in Fig. 21(b), we plot the  $dR(T)/dT$  of the same data. The 10 kOe transition temperature data are also plotted in Fig. 20; it can be seen that (i) the field dependence of the ambient pressure data is consistent with the  $T$ - $H$  phase diagram for  $H_{\parallel c}$  shown in Fig. 7(a) (i.e., the  $T_2$  line being much more sensitive to 10 kOe than either the  $T_1$  or  $T_3$  line) and (ii) that there is very little change in the transition temperatures with pressure at either 0 or 10 kOe.

## V. DISCUSSION

The growth of large single-crystalline samples of  $\text{La}_2\text{Ni}_7$  has allowed for zero-field measurements of  $\rho(T)$  and  $C_p(T)$  combined with low-field measurements of  $M(T)/H$  to identify

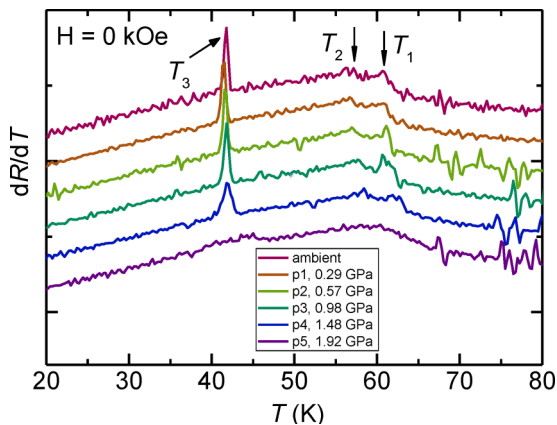


FIG. 19.  $dR(T)/dT$  plots for  $\text{La}_2\text{Ni}_7$  under pressure for  $p < 2.0$  GPa for  $20 \text{ K} < T < 80 \text{ K}$  based on the data shown in Fig. 18.

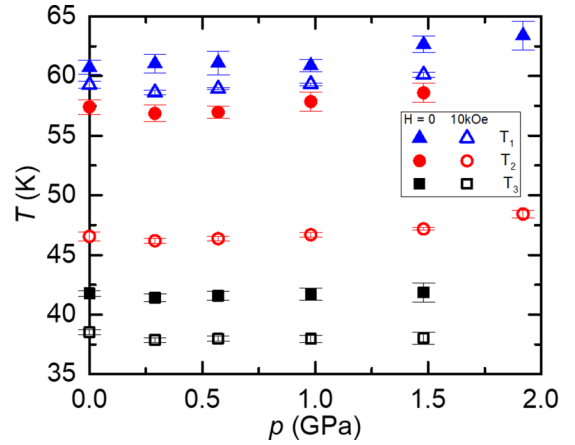


FIG. 20.  $T$ - $p$  phase diagram for  $\text{La}_2\text{Ni}_7$  for  $H = 0$  (solid points) and  $H_{\parallel c} = 10$  kOe (open points).

three zero (or low)-field magnetic phase transition temperatures  $T_1 = 61.0 \pm 0.2 \text{ K}$ ,  $T_2 = 56.5 \pm 0.2 \text{ K}$ , and  $T_3 = 42.2 \pm 0.2 \text{ K}$ . Detailed anisotropic  $M(T, H)$  and  $\rho(T, H)$  measurements have allowed for the construction of anisotropic  $H$ - $T$  phase diagrams, revealing multiple regions, labeled A-F in Figs. 7(a) and 7(b). Whereas phases A and B appear to be AFM in nature, phase C clearly has some FM component,

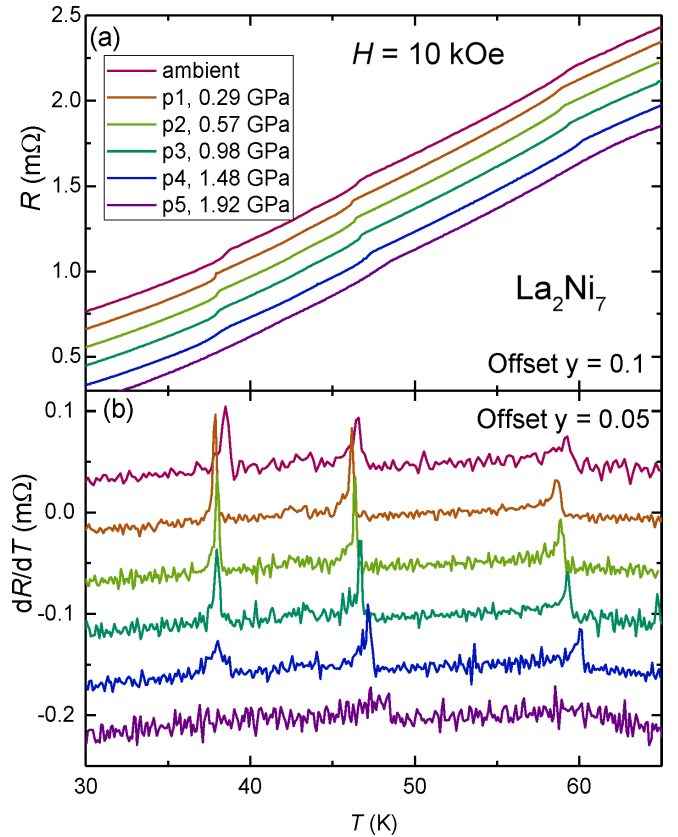


FIG. 21. (a)  $R(T)$  for  $\text{La}_2\text{Ni}_7$  for  $30 \text{ K} < T < 65 \text{ K}$  with a magnetic field of  $H_{\parallel c} = 10$  kOe; data curves are offset from each for clarity. (b)  $dR/dT$  plots of the data shown in (a); data curves are offset from each for clarity.

most likely combined with some finite- $q$  ordering vector. The low-temperature saturated moment of  $\sim 0.12 \mu_B/\text{Ni}$  as well as the very small change in entropy associated with the features in specific heat suggest itinerant, small-moment ordering. This is further supported if we follow the Rhodes-Wohlfarth [43] analysis outlined in Ref. [22]. The parameter is  $\mu_c/\mu_{\text{sat}}$  where  $\mu_{\text{eff}}^2 = \mu_c(\mu_c + 2\mu_B)$ ; if we use our  $\mu_{\text{eff}} = 1.3 \mu_B/\text{Ni}$  and our  $\mu_{\text{sat}} = 0.12 \mu_B/\text{Ni}$ , we find  $\mu_c = 0.64 \mu_B/\text{Ni}$  and  $\mu_c/\mu_{\text{sat}} = 5.3$ , which is consistent with an itinerant system.

Although the experimental reality of  $\text{La}_2\text{Ni}_7$  is much more complex than a single transition to an AFM ground state, it is useful to compare our results with recent band structural work. In their study of  $\text{La}_2\text{Ni}_7$  and  $\text{Y}_2\text{Ni}_7$ , Crivello and Paul-Boncour [24] used electronic band structure calculations to gain insight into their magnetically ordered states. For both compounds, they found that a FM state was the most stable low-temperature state, with a lowering of total energy by 5 meV/Ni for each compound. In addition, the ordered moments were found to favor alignment along the crystallographic  $c$  axis. This is consistent with a FM transition of  $\sim 50$  K in  $\text{Y}_2\text{Ni}_7$  but clearly is not consistent with the AFM ground state found for  $\text{La}_2\text{Ni}_7$ . For  $\text{La}_2\text{Ni}_7$ , there was a nearby (energetically) AFM state with blocks of Ni moments aligned parallel and antiparallel to the  $c$  axis. The energy difference between this AFM state and the FM state is  $< 1$  meV/Ni and considered within the accuracy of the density functional theory (DFT) calculations. As such, Crivello and Paul-Boncour [24] claim that both magnetic structures present the same stability at 0 K. Given that the FM blocks that make up the computationally predicted AFM state consist of six layers of Ni atoms that are FM aligned, our measured paramagnetic  $\theta$  of  $-55$  K (as opposed to a positive value for a simple AFM) is not too disconcerting [24]. Of course, the fact that we have determined that the highest temperature C phase has a clear FM component to its ordering provides an experimental rationale for the sign of  $\theta$  as well.

Although the computational work only examines a single magnetically ordered state, these band structure results are consistent with several aspects of our data. Given the computational degeneracy between AFM and FM states for  $\text{La}_2\text{Ni}_7$ , the multiple zero-field transitions as well as field-induced transitions are not surprising. Indeed, the C phase shown in Figs. 7(a) and 7(b) has a clear net FM component that is replaced at lower temperatures by the AFM states in the B and A phases. In addition, the measured linear component of the temperature-dependent specific heat  $C_p/T$ ,  $\gamma = 40 \text{ mJ}/(\text{mol K}^2)$ , is somewhat enhanced and is consistent with the computationally predicted enhanced DOS at  $E_F$ . Finally, our anisotropic  $M(T)$  and  $M(H)$  data demonstrate that the ordered moments (in low fields) are aligned along the  $c$  axis. As will be discussed below, the low-field alignment of the moments along the crystallographic  $c$  axis is even further demonstrated a clear spin-flop transition that is associated with the D phase.

The pressure insensitivity of all three magnetic phase transitions is rather surprising for such a small-moment AFM ordering where, naively, some degree of fragility might be anticipated. These results suggest that  $\text{La}_2\text{Ni}_7$  may be rather incompressible, and indeed, DFT-based band structure calculations, conducted using the PBE exchange-correlation

functional [44], suggest (qualitatively) that  $\text{La}_2\text{Ni}_7$  has a significantly larger bulk modulus than either  $\text{EuCd}_2\text{As}_2$  or  $\text{LaCrGe}_3$  [45], two recently studied compounds with well-defined pressure dependences [9–11,46]. Whereas our results for applied pressures up to 2 GPa clearly suggest the need for higher pressure measurements, our current data also suggest that this may be increasingly difficult, given the subtlety of the features in resistivity, the smallness of the features in specific heat, and the difficulty of measuring and tracking AFM phase transitions with magnetization measurements for pressures  $> 2$  GPa. Empirically, a comparison of  $\text{La}_2\text{Ni}_7$  and  $\text{Y}_2\text{Ni}_7$  offers mixed signals. The crystal structures are similar, and there is some contraction of the volume per formula unit (consistent with a degree of positive chemical pressure). The transition temperatures of the two compounds are similar (implying a perhaps weak pressure dependence in ordering temperature), but the saturated moment size in  $\text{Y}_2\text{Ni}_7$  is roughly a factor of two smaller than in  $\text{La}_2\text{Ni}_7$  (both experimentally and computationally) [24,47]. Further theoretical/computational insight may be possible if neutron scattering measurements can determine the ordering wave vector associated with each of the zero-field regions. Application of pressure *in silico* (computationally) may provide some insight as to what higher pressures will do, especially if the same simulations can capture the current ambient pressure magnetic structures and their pressure dependences.

Having constructed the phase diagrams shown in Figs. 7(a) and 7(b), we can see that there are clear similarities and differences. At the grossest level, the two  $H$ - $T$  phase diagrams can be understood by observing that there have to be three zero-field transition temperatures with  $(H, T)$  lines emerging from them at low fields, and at high fields, as we approach  $T = 0$  K, there are two critical fields with  $(H, T)$  lines emerging from them. At intermediate temperatures and fields, a more complex geometry of  $(H, T)$  lines emerge. There are two clear  $(H, T)$  lines: one runs from  $T_1$  to what is labeled as  $H_1$ , the highest metamagnetic field at base temperature; the other runs from  $T_3$  to the lower metamagnetic field at base temperature (and labeled as  $H_3$ ). As we go from  $H_{\parallel c}$  to  $H_{\perp c}$ , both  $H_1$  and  $H_3$  increase with  $H_3$  increasing by a much larger percentage, i.e., drawing closer to  $H_1$ . Whereas for  $H_{\parallel c}$ , there are four rather well-defined  $H$ - $T$  regions (with the open question of what is the nature of the apparent line between the low-field  $T_1$  and  $T_2$  lines that itself does not reach down to  $H = 0$ ), for  $H_{\perp c}$ , there appear to be five, with a skinny, lenticular region marked as F existing between the  $T_1$  and  $T_3$  lines at intermediate fields and temperatures.

Whereas the three regions that extend down to  $H = 0$  [A, B, and C in both Figs. 7(a) and 7(b)] are associated with the same ordered states in the two phase diagrams, at least at lowest fields, the regions that exist only at finite fields (D, E, and F) are not inherently related. This said, we can compare the  $M(H)$  data for  $H_{\parallel c}$  and  $H_{\perp c}$  from Figs. 8 and 10. Figure 22 shows data for  $T = 15$  K; for fields  $< 30$  kOe, we can see a clear anisotropy in the  $M(H)$  with  $H_{\perp c}$  having a significantly larger slope. This is consistent with the computational prediction that the low-temperature AFM ordered phase has the Ni moments aligned along the  $c$  axis direction. For higher fields applied along the  $c$  axis, the data shown in Fig. 22 are a classic example of a spin-flop transition [48,49]. As such, these data

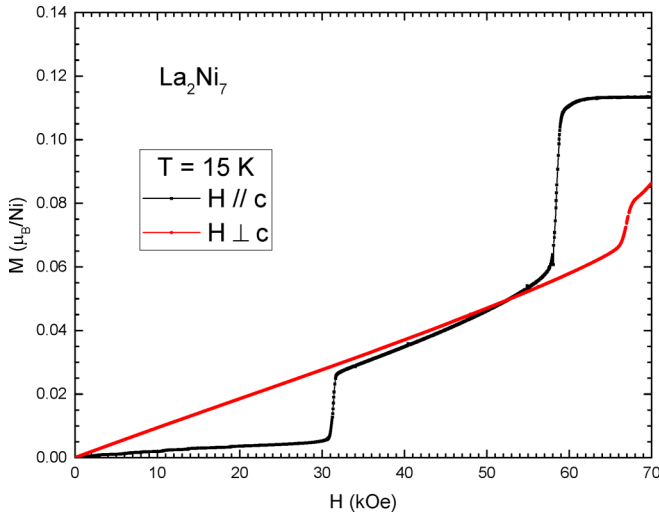


FIG. 22. Anisotropic  $H_{\parallel c}$  and  $H_{\perp c}$   $M(H)$  data for  $T = 15$  K.

strongly suggest that, for  $H_{\parallel c}$ , the D phase has a similar arrangement of ordered moments as does the A phase but with their orientation rotated by  $\sim 90^\circ$ . In this scenario then, the ordered moments in the D phase maintain AFM ordering but are aligned to be roughly perpendicular to the  $c$  axis. In Fig. 22 then, for  $32 \text{ kOe} < H < \sim 56 \text{ kOe}$ , for  $H_{\parallel c}$  (D phase) and for  $H_{\perp c}$  (A phase), the  $M(H)$  data are associated with an AFM order that is aligned roughly perpendicular to the respective applied field.

Whereas the D phase appears to be AFM in nature, the metamagnetic E phase for  $H_{\perp c}$  (seen in Fig. 22 for  $H_{\perp c} \sim > 64 \text{ kOe}$  as well as Fig. 10 for other temperatures) likely has a FM component to the order, i.e., the magnetic unit cell has a finite magnetization value. Clearly, neutron scattering will be needed to determine the wave vectors associated with each of the phases identified in the phase diagrams delineated in Fig. 7.

The data shown in Fig. 22, in addition to providing some insight into the nature of the D phase, can also be used to extract some initial estimates of the exchange field  $H_E$  and uniaxial anisotropy field  $H_A$  within the basis of the two sublattice Néel models [48,49]. Given that  $\text{La}_2\text{Ni}_7$  is clearly a small-moment itinerant system with potentially complex order, i.e., having more than two sublattices, this analysis may be questionable, but it can at least provide some context. If we use the formalism presented by Holmes *et al.* [48], take the spin-flop field to be 31 kOe, take the saturated moment at high fields to be  $0.12 \mu_B/\text{Ni}$ , and take the anisotropic susceptibilities to be the two slopes of the nearly linear  $M(H)$  data shown in Fig. 22 for fields  $< 30 \text{ kOe}$  (giving  $\chi_{\parallel} = 1.72 \times 10^{-4} \mu_B/(\text{Ni kOe})$  and  $\chi_{\perp} = 9.38 \times 10^{-4} \mu_B/(\text{Ni kOe})$ ) and assume that  $H_A$  is small compared with  $H_E$  (as was done in Ref. [48]), we can infer that  $H_E$  is 125 kOe and  $H_A$  is

3 kOe. These values may provide some benchmark for future computational or neutron scattering efforts to better model or understand the finer details of the  $\text{La}_2\text{Ni}_7$  structures.

In summary, we have determined three zero-field magnetic transition temperatures for  $\text{La}_2\text{Ni}_7$ :  $T_1 = 61.0 \pm 0.2 \text{ K}$ ,  $T_2 = 56.5 \pm 0.2 \text{ K}$ , and  $T_3 = 42.2 \pm 0.2 \text{ K}$ . These magnetically ordered phases are associated with small moments ( $\sim 0.12 \mu_B/\text{Ni}$  in the saturated state) and small changes in entropy. Remarkably,  $T_1$ ,  $T_2$ , and  $T_3$  are relatively pressure insensitive (i.e., changing by  $< 3 \text{ K}$ ) for applied pressures up to 2 GPa. We have determined anisotropic  $H$ - $T$  phase diagrams for  $H_{\parallel c}$  and  $H_{\perp c}$ . We have identified the ground state phase A as being AFM with the moments aligned along the  $c$  axis. For  $H_{\parallel c}$ , as the applied field is increased to  $> \sim 33 \text{ kOe}$ , the metamagnetic D phase appears to be a spin-flop state with the ordered moments still AFM aligned but now perpendicular to the applied field. Whereas the B phase appears to be AFM ordered, the highest temperature low-field C phase has a clear FM component. The E and F phases also have net FM components.

Given the wealth of detail that our single-crystal measurements have provided, multiple follow-up measurements and experiments are suggested. Whereas neutron scattering measurements were tried on polycrystalline materials [20] and failed to detect any new wave vectors associated with the onset of AFM order, clearly, new measurements on single-crystalline samples are needed. With the information from this paper as well as (potentially) ordering wave vectors from scattering measurements, band structural calculations should be revisited and revised using the details outlined in this paper to refine modeling of the magnetism in  $\text{La}_2\text{Ni}_7$ . In addition to these efforts, temperature-dependent nuclear magnetic resonance (NMR) as well as angle resolved photoemission spectroscopy (ARPES) measurements are possible. Both NMR and ARPES can also shed light on the nature of the magnetic order and how it impacts the band structure.

## ACKNOWLEDGMENTS

We thank Linlin Wang for providing relative values of the compressibility  $\text{La}_2\text{Ni}_7$ ,  $\text{LaCrGe}_3$ , and  $\text{EuCd}_2\text{As}_2$  [45]. This work was supported by the U.S. Department of Energy, Office of Basic Energy Science, Division of Materials Sciences and Engineering. The research was performed at the Ames Laboratory. Ames Laboratory is operated for the U.S. Department of Energy by Iowa State University under Contract No. DE-AC02-07CH11358. D.H.R. was supported in part by U.S. Department of Energy, Office of Basic Energy Science, Division of Materials Sciences and Engineering under Contract No. DE-AC02-07CH11358; financial support for D.H.R. was also provided by Fonds Québécois de la Recherche sur la Nature et les Technologies and the Natural Sciences and Engineering Research Council (NSERC) Canada. R.A.R. was supported in part by the Gordon and Betty Moore Foundation's EPIQS Initiative through Grant No. GBMF4411.

[1] P. C. Canfield and S. L. Bud'ko, *Rep. Prog. Phys.* **79**, 084506 (2016).

[2] D. Belitz, T. R. Kirkpatrick, and T. Vojta, *Phys. Rev. B* **55**, 9452 (1997).

- [3] A. V. Chubukov, C. Pépin, and J. Rech, *Phys. Rev. Lett.* **92**, 147003 (2004).
- [4] G. J. Conduit, A. G. Green, and B. D. Simons, *Phys. Rev. Lett.* **103**, 207201 (2009).
- [5] U. Karahasanovic, F. Krüger, and A. G. Green, *Phys. Rev. B* **85**, 165111 (2012).
- [6] S. J. Thomson, F. Krüger, and A. G. Green, *Phys. Rev. B* **87**, 224203 (2013).
- [7] C. J. Pedder, F. Krüger, and A. G. Green, *Phys. Rev. B* **88**, 165109 (2013).
- [8] G. Abdul-Jabbar, D. A. Sokolov, C. D. O'Neill, C. Stock, D. Wermeille, F. Demmel, F. Krüger, A. G. Green, F. Levy-Bertrand, B. Grenier, and A. D. Huxley, *Nat. Phys.* **11**, 321 (2015).
- [9] V. Taufour, U. S. Kaluarachchi, R. Khasanov, M. C. Nguyen, Z. Guguchia, P. K. Biswas, P. Bonfà, R. De Renzi, X. Lin, S. K. Kim, E. D. Mun, H. Kim, Y. Furukawa, C.-Z. Wang, K.-M. Ho, S. L. Bud'ko, and P. C. Canfield, *Phys. Rev. Lett.* **117**, 037207 (2016).
- [10] U. S. Kaluarachchi, S. L. Bud'ko, P. C. Canfield, and V. Taufour, *Nat. Commun.* **8**, 546 (2017).
- [11] E. Gati, J. M. Wilde, R. Khasanov, L. Xiang, S. Dissanayake, R. Gupta, M. Matsuda, F. Ye, B. Haberl, U. Kaluarachchi, R. J. McQueeney, A. Kreyssig, S. L. Bud'ko, and P. C. Canfield, *Phys. Rev. B* **103**, 075111 (2021).
- [12] L. Xiang, E. Gati, S. L. Bud'ko, S. M. Saunders, and P. C. Canfield, *Phys. Rev. B* **103**, 054419 (2021).
- [13] U. S. Kaluarachchi, L. Xiang, J. Ying, T. Kong, V. Struzhkin, A. Gavriluk, S. L. Bud'ko, and P. C. Canfield, *Phys. Rev. B* **98**, 174405 (2018).
- [14] U. S. Kaluarachchi, V. Taufour, S. L. Bud'ko, and P. C. Canfield, *Phys. Rev. B* **97**, 045139 (2018).
- [15] A. V. Virkar and A. Raman, *J. Less Comm. Met.* **18**, 59 (1969).
- [16] K. H. J. Buschow, *J. Mag. Mag. Mater.* **40**, 224 (1983).
- [17] F. T. Parker and H. Oesterreicher, *J. Less Comm. Met.* **90**, 127 (1983).
- [18] U. Gottwick, K. Gloos, S. Horn, F. Steglich, and N. Grewe, *J. Mag. Mag. Mater.* **47–48**, 536 (1985).
- [19] Y. Tazuke, R. Nakabayashi, S. Murayama, T. Sakakibara, and T. Goto, *Physica B* **186–188**, 596 (1993).
- [20] Y. Tazuke, M. Abe, and S. Funahashi, *Physica B* **237–238**, 559 (1997).
- [21] M. Fukase, Y. Tazuke, H. Mitamura, T. Goto, and T. Sato, *J. Phys. Soc. Japan* **68**, 1460 (1999).
- [22] M. Fukase, Y. Tazuke, H. Mitamura, T. Goto, and T. Sato, *Mater. Trans. JIM* **41**, 1046 (2000).
- [23] Y. Tazuke, H. Suzuki, and H. Tanikawa, *Physica B* **346–347**, 122 (2004).
- [24] J.-C. Crivello and V. Paul-Boncour, *J. Phys.: Condens. Matter* **32**, 145802 (2020).
- [25] P. C. Canfield and I. R. Fisher, *J. Cryst. Growth* **225**, 155 (2001).
- [26] P. C. Canfield, *Rep. Prog. Phys.* **83**, 016501 (2020).
- [27] A. C. Larson and R. B. Von Dreele, General Structure Analysis System (GSAS), Los Alamos National Laboratory Report LAUR 86-748 (Los Alamos National Laboratory, Los Alamos, 2004), <https://11bm.xray.aps.anl.gov/documents/GSASManual.pdf>.
- [28] B. H. Toby, *J. Appl. Cryst.* **34**, 210 (2001).
- [29] P. Villars, H. Okamoto, and K. Cenzual, ASM Alloy Phase Diagram Database Online, No. 1600322, [https://www.asminternational.org/materials-resources/online-databases/-/journal\\_content/56/10192/15469013/DATABASE](https://www.asminternational.org/materials-resources/online-databases/-/journal_content/56/10192/15469013/DATABASE).
- [30] H. Okamoto, *J. Phase Equilib.* **23**, 287 (2002).
- [31] J. Dischinger and H. J. Schaller, *J. Alloys Compd.* **312**, 201 (2000).
- [32] Z. Deyuan, J. Tang, and K. A. Gschneidner Jr., *J. Less Comm. Metals* **169**, 45 (1991).
- [33] S. L. Bud'ko, A. N. Voronovskii, A. G. Gapotchenko, and E. S. Itskevich, *Zh. Eksp. Teor. Fiz.* **86**, 778 (1984) [*Sov. Phys. JETP* **59**, 454 (1984)].
- [34] S. K. Kim, M. S. Torikachvili, E. Colombier, A. Thaler, S. L. Bud'ko, and P. C. Canfield, *Phys. Rev. B* **84**, 134525 (2011).
- [35] M. S. Torikachvili, S. K. Kim, E. Colombier, S. L. Bud'ko, and P. C. Canfield, *Rev. Sci. Instrum.* **86**, 123904 (2015).
- [36] B. Bireckoven and J. Wittig, *J. Phys. E* **21**, 841 (1988).
- [37] L. Xiang, E. Gati, S. L. Bud'ko, R. A. Ribeiro, A. Ata, U. Tutsch, M. Lang, and P. C. Canfield, *Rev. Sci. Instrum.* **91**, 095103 (2020).
- [38] M. E. Fisher and J. S. Langer, *Phys. Rev. Lett.* **20**, 665 (1968).
- [39] M. E. Fisher, *Philos. Mag.* **7**, 1731 (1962).
- [40] R. A. Ribeiro, S. L. Bud'ko, and P. C. Canfield, *J. Magn. Magn.* **267**, 216 (2003).
- [41] T. A. Wiener and P. C. Canfield, *J. Alloys Compd.* **303**, 505 (2000).
- [42] T. Kong, C. Cunningham, V. Taufour, S. L. Bud'ko, M. L. C. Buffon, X. Lin, H. Emmons, and P. C. Canfield, *J. Magn. Magn.* **358**, 212 (2014).
- [43] P. Rhodes and E. P. Wohlfarth, *Proc. R. Soc. Lond. A* **273**, 247 (1963).
- [44] J. P. Perdew, K. Burke, and M. Ernzerhof, *Phys. Rev. Lett.* **77**, 3865 (1996).
- [45] Although PBE values of compressibility are likely smaller than experimental values, for relative comparison, it can provide some insight. The values found were 115, 88, and 45 GPa for  $\text{La}_2\text{Ni}_7$ ,  $\text{LaCrGe}_3$ , and  $\text{EuCd}_2\text{As}_2$ , respectively.
- [46] E. Gati, S. L. Bud'ko, L. Wang, A. Valadkhani, R. Gupta, B. Kuthanazhi, L. Xiang, J. M. Wilde, A. Sapkota, Z. Guguchia, R. Khasanov, R. Valenti, and P. C. Canfield, *Phys. Rev. B* **104**, 155124 (2021).
- [47] A. Bhattacharyya, D. Jain, V. Ganesan, S. Giri, and S. Majumdar, *Phys. Rev. B* **84**, 184414 (2011).
- [48] L. Holmes, M. Eibschutz, and H. J. Guggenheim, *Solid State Commun.* **7**, 973 (1969).
- [49] T. Nagamiya, K. Yosida, and R. Kubo, *Adv. Phys.* **4**, 1 (1955).